

SPECTROSCOPIC DETECTION OF TURBULENCE IN POST-CME CURRENT SHEETS

A. BEMPORAD¹

Received 2008 April 12; accepted 2008 August 10

ABSTRACT

Plasma in post-CME current sheets (CSs) is expected to be highly turbulent because of the tearing and coalescence instability and/or local microscopic instabilities. For this reason, in the last decade the inconsistency between the observed ($\sim 10^4$ – 10^5 km) and the expected (~ 1 – 10 m) CS thickness has been tentatively explained in many MHD models as a consequence of plasma turbulence that should be able to significantly broaden the CS. However, from the observational point of view, little is known about this subject. A few post-CME CSs have been observed in UVCS spectra as a strong emission in the high-temperature [Fe xviii] line, usually unobservable in the solar corona. In this work, published data on post-CME CSs observed by UVCS are reanalyzed, concentrating for the first time on the evolution of turbulence derived from the nonthermal broadening of the [Fe xviii] line profiles. Derived turbulent speeds are on the order of ~ 60 km s⁻¹ a few hours after the CME and slowly decay down to ~ 30 km s⁻¹ in the following 2 days. From this evolution the anomalous diffusivity due to microinstabilities has been estimated, and the scenario of multiple small-scale reconnections is tested. Results show that the existence of many ($\sim 10^{-11}$ to 10^{-17} μ CS m⁻³) microscopic CSs (μ CSs) of small sizes (~ 10 – 10^4 m) could explain not only the high CS temperatures but also the much larger observed thickness of macroscopic CSs, thanks to turbulent broadening.

Subject headings: Sun: corona — Sun: coronal mass ejections (CMEs) — Sun: UV radiation — turbulence

1. INTRODUCTION

In the last decade spectroscopic UV observations of coronal mass ejections (CMEs) acquired by the Ultraviolet Coronagraph Spectrometer (UVCS; Kohl et al. 1995) on board the *Solar & Heliospheric Observatory* (SOHO) spacecraft strongly increased our knowledge of plasma temperatures, densities, abundances in the CME cores and leading edges, and their 3D structure from velocities inferred from observed spectral line Doppler shifts and Doppler dimmings (see Kohl et al. [2006] for a review of UVCS observations of CMEs). Several analyses based on UVCS data on the limb events focused on the study of post-CME current sheets (CSs), whose formation in the eruption was predicted by both breakout and flux rope CME models (see, e.g., Lin & Forbes 2000; Amari et al. 2003). Post-CME CSs, usually identified in white-light images acquired by the Large Angle and Spectrometric Coronagraph (LASCO; Brueckner et al. 1995) as radial structures aligned with the CME latitude (see, e.g., Webb et al. 2003), are characterized in UVCS spectra by the presence of an unusual high-temperature emission in the [Fe xviii] $\lambda 974.8$ spectral line; the very high temperature of maximum formation $T_{\max} \simeq 5 \times 10^6$ K of this line makes it usually unobservable in the $\sim 10^6$ K solar corona. In some works this emission has been observed only in the first few minutes (Raymond et al. 2003; Lee et al. 2006) or hours (Ciaravella et al. 2002) after the eruption, but other observations demonstrated that [Fe xviii] emission may last for even more than 2 days after the CME (Ko et al. 2003; Bemporad et al. 2006). More recently, Ciaravella & Raymond (2008) reported on the first CS that was observed in UV from its onset whose spectra show a [Fe xviii] emission lasting for ≈ 7 hr after the CME.

The reason for these large differences in the duration of [Fe xviii] emission is at present unclear. Reconnection models predict that, after the eruption, plasma heated and accelerated at chromospheric and low coronal levels in the diffusion region (i.e., where

the reconnection of coronal fields occurs, hereafter DR) is ejected outward along the CS and inward toward the top of post-CME loops, where a fast shock occurs, generating hard X-ray emission (see review by Aschwanden 2002). In agreement with this picture, previous UVCS papers ascribed the observed long-lasting [Fe xviii] emission to the high-temperature CS plasma heated in the DR and observed as it crosses the spectrometer slit field of view. However, the interpretation for the observed [Fe xviii] emission is not straightforward. UVCS has observed this line typically at heliocentric distances ranging between ~ 1.5 and $1.7 R_{\odot}$, and it is not always easy to understand from observations in different events if the altitude of the UVCS projected field of view was either below the cusp of closed loops, or above it in the DR, or maybe even above the DR. In any case, there is a general consensus that [Fe xviii] emission originates *above* the cusp of post-CME loops probably in the DR, as indirectly concluded by previous authors from considerations on many observational parameters such as elemental abundances and emission measure (Ko et al. 2003), plasma cooling rate and post-CME loops rising speed (Bemporad et al. 2006), 3D reconstruction of CME material expansion (Lee et al. 2006), and outflowing mass flux conservation (Ciaravella & Raymond 2008).

Despite the progress made in the knowledge of CS properties, from the theoretical point of view many problems are still open: First, even if we assume that the high-temperature plasma observed by UVCS originated at the DR, the fast Petscheck-type (Petscheck 1964) magnetic reconnection envisaged in flare-CME models occurring at the DR should be able also to explain the observed long duration of post-CME CSs and the $\sim 5 \times 10^6$ K emission lasting in the corona even for days after the eruption. It is in fact at present unclear how reconnection occurring in the DR could explain at the same time a hard X-ray emission at the top of post-eruption loops that fades typically in a few minutes (see, e.g., Petrosian et al. 2002) and the high-temperature emission in CSs that fades in a few days unless a transition from Petscheck to Sweet-Parker reconnections occur. Moreover, numerical simulations (e.g., Biskamp 1986) show that, if the resistivity is spatially uniform, a steady Petscheck-type reconnection cannot

¹ INAF–Torino Astronomical Observatory, Via Osservatorio 20, 10025 Pino Torinese (TO), Italy.

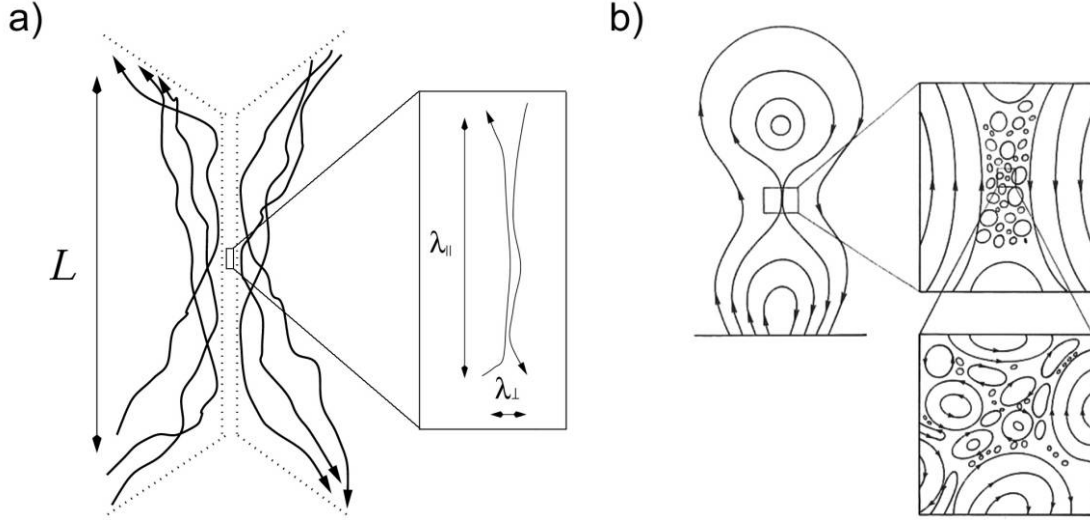


FIG. 1.— Two cartoons showing (a) the concept of stochastic reconnection (adapted from Lazarian & Vishniac 1999) and (b) fractal reconnection (adapted from Tajima & Shibata 1997, p. 242) in CSs. (a) In the Lazarian & Vishniac (1999) model a stochastic component is added to a magnetic field globally reconnecting over the length scale L and induces local Sweet-Parker type reconnections at much shorter scales λ_{\parallel} , $\lambda_{\perp} \ll L$. (b) In the Tajima & Shibata (1997, p. 242) model the CS stretching leads, via scale-free secondary tearing and coalescence processes, to the formation of many magnetic islands of different sizes and hence to a fractal CS structure.

be produced because it evolves toward a slow Sweet & Parker-type reconnection (Sweet 1958; Parker 1957). Kulsrud (2001) demonstrated that for spatially uniform resistivity, the Petscheck-type reconnection mathematically reduces to the Sweet & Parker-type reconnection. Steady Petscheck-type reconnection requires a localized resistivity such as the “anomalous resistivity.” Laboratory plasma experiments (e.g., Hsu et al. 2000) show that the ion heating observed during collisionless reconnection (i.e., when the mean free path is much longer than the CS thickness) can be explained only by introducing an anomalous resistivity much larger than the classical one; microscopic instabilities inducing plasma turbulence are expected to be able to produce such resistivity. However, this implies a second problem; laboratory plasma experiments (see review by Yamada 1999) showed that anomalous resistivity can be produced only if the CS thickness is as small as the ion Larmor radius

$$r_L = \frac{m_i v_{th}}{eB} \simeq 10^{-2} \frac{\sqrt{T_i}}{B} \text{ m} \quad (1)$$

where m_i is the ion (i.e., proton) mass, $v_{th} = (2k_B T_i / m_i)^{1/2}$ is the thermal velocity, T_i is the ion kinetic temperature, and $B(\text{G})$ is the magnetic field that is on the order of a few meters in the solar corona, while the observed post-CME CS thickness D_{obs} is typically on the order of $D_{obs} \sim 10^4 - 10^5$ km. The large observed CS thickness is also related to a further huge-scale gap present between the expected (η_{exp}) and the inferred (η_{obs}) CS plasma diffusivities.² In order to produce a stationary CS of thickness D_{obs} , a balance is required between inflow of plasma occurring with velocity $V_{in} \sim 10$ km s⁻¹ and the CS diffusion η/D , so that $\eta_{obs} = V_{in} D_{obs} \sim 10^{11} - 10^{12}$ m² s⁻¹. This value is much larger than classical diffusivity $\eta_c \sim 10^9 T^{-3/2} \sim 1$ m² s⁻¹ in the $\sim 10^6$ K solar corona and anomalous diffusivity³ that is on the order of $10^6 - 10^7$ m² s⁻¹ (see also discussion in Lin et al. 2007). These

² I remind the reader that the magnetic diffusivity η_d (m² s⁻¹) and the resistivity η_r (Ωm) are simply related to each other by $\eta_d = \eta_r / \mu_0$, where $\mu_0 = 4\pi \times 10^{-7}$ Hm⁻¹ is the permeability of free space.

³ In the hypothesis of ion-acoustic turbulence; see § 5.

inconsistencies pose serious challenges to the existing theories of magnetic reconnection.

Plasma turbulence has been proposed as a possible solution; it is well known that vertically elongated CSs are unstable mainly via tearing and/or Kelvin-Helmholtz instabilities⁴ that may produce magnetic islands (in 2D, or flux ropes in 2.5D) via successive reconnections and lead the plasma toward a turbulent state. Tearing mode turbulence can produce a much higher resistivity, usually referred to as “hyperresistivity” (Strauss 1986, 1988), that could be more important than the resistivity produced by micro-instabilities and significantly broaden the CS. However, such instability leads to a CS diffusion $\sim 10^9$ times larger than that implied by anomalous lower hybrid drift diffusivity (see also discussion in Lin et al. 2007) and does not allow the evading of the constraints on the global plasma flow that lead to slow reconnection speeds, as has been demonstrated analytically (Lazarian & Vishniac 1999) and numerically (Matthaeus & Lamkin 1985). Alternatively, Lazarian & Vishniac (1999) proposed a reconnection model where a stochastic component of magnetic field leads to multiple small-scale local reconnections that result in a fast reconnection rate even when the local inflow speed is slow (Fig. 1a); an important distinction between *global* and *local* reconnection rates is made. Turbulent reconnection models are still under debate. For instance, Kim & Diamond (2001) concluded that the effect of hyperresistivity is negligible with respect to turbulent diffusivity and that, despite turbulence, the global reconnection rate (that scales as in the Sweet & Parker-type reconnection) cannot be given by a simple sum of local reconnection events (as claimed by Lazarian & Vishniac 1999); hence, fast global reconnection cannot be achieved. It has also been proposed that, as the CS is stretched with the CME propagation, recurrent secondary tearing instabilities occurring at different spatial scales lead to a fractal (i.e., scale-free) CS structure (Fig. 1b), where many magnetic islands of different sizes (subject also to coalesce each other) connect macroscopic and microscopic scales and fill the scale gap mentioned above (see Tajima & Shibata 1997, p. 242; Shibata & Tanuma 2001). The main idea is that energy is supplied at the largest spatial scales being redistributed via MHD

⁴ Rayleigh-Taylor instability is usually important only for horizontal CSs.

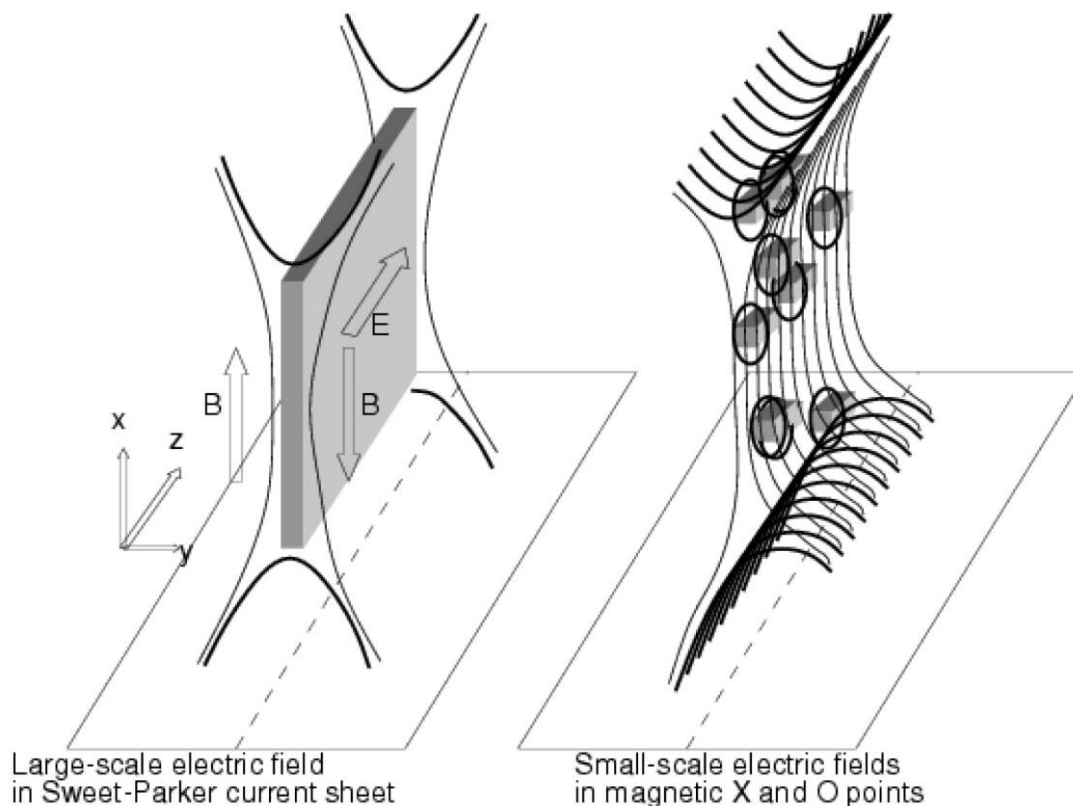


FIG. 2.—Paradigm shift of CS structure. Theory and simulations demonstrate that the classical Sweet-Parker CS (*left*) becomes unstable via tearing, leading to a fragmented topology with many small-scale magnetic islands (*right*; from Aschwanden 2002).

turbulent cascade to smaller scales and finally dissipated, as suggested by the model originally proposed for solar flares by LaRosa & Moore (1993).

A problem with different turbulent reconnection models is that, at present, there are no clear observational constraints that can be used to distinguish between them. As also pointed out by Aschwanden (2002), the existence of small-scale reconnecting regions in flare CSs (Fig. 2) is predicted theoretically (because stretched Sweet-Parker CSs undergo tearing instability, leading to the formation of magnetic islands), but is also corroborated observationally. In fact, although direct observation of such small scales is at present impossible,⁵ hard X-ray and radio emissions observed during solar flares and type III bursts have many properties that have been ascribed to the existence of small-scale, fragmented, “bursty” magnetic reconnections such as radio frequency drift pairs, the slope of X-ray emission wavelet power spectra, and the fast (\sim subsecond) time structure of hard X-ray and radio pulses (see review by Aschwanden 2002). Recently, Huang & Lin (2006) interpreted the quasi-periodic oscillations observed in radio polarization data during a solar flare as the signature of a series of elementary energy-release processes injecting energetic electrons.

Despite the importance of turbulence discussed above in magnetic reconnection theories, from the observational point of view plasma turbulence in post-CME CSs has thus far never been studied. This work concentrates on this subject; information on plasma turbulence in post-CME CSs is derived here by studying

the evolution of the [Fe XVIII] line profiles in UVCS data sets already studied by Ciaravella et al. (2002), Ko et al. (2003), Raymond et al. (2003), Bemporad et al. (2006), Lee et al. (2006), and Ciaravella & Raymond (2008). In these works the authors focus on the CS plasma temperatures, densities, and elemental abundances, but there is little information on the [Fe XVIII] line profiles. After a general discussion on the determination of turbulence velocity from line profile widths (§ 2), results obtained from the study of [Fe XVIII] profiles in all the post-CME CS reported so far with this line are described in § 3. The following analysis concentrates on the event of 2002 November 26 (Bemporad et al. 2006, hereafter Paper I), the only one for which ~ 2.3 days of continuous [Fe XVIII] data are available; additional CS plasma parameters derived from energy balance (§ 4) are used in the following sections (§ 5) to estimate local anomalous resistivities in the hypothesis of ion-acoustic (§ 5.1) and lower hybrid drift (§ 5.2) instabilities. In the scenario of fractal reconnection, physical information on local reconnecting micro-CSs (e.g., the size of “microscopic” reconnection regions and local reconnection rates; § 6) are derived. These results are discussed in § 7, where it is shown how micro-CSs are also able to explain globally the high CS plasma temperatures and the much larger observed CS thickness, suggesting from the observational point of view a possible scenario to explain part of the theoretical problems discussed above.

2. ESTIMATE OF NONTHERMAL VELOCITIES FROM SPECTRAL LINE PROFILES

As mentioned in § 1, post-CME CSs plasma can be highly turbulent due to the occurrence of tearing and coalescence instabilities and/or microscopic instabilities. If nonthermal motions are occurring with a rms velocity v_{Nth} , the effective profile FWHM

⁵ The expected size of elementary acceleration cells in solar flares is believed to be on the order of $\approx 10^2 - 10^3$ m (see Aschwanden et al. 1998), i.e., $\approx 10^{-3}$ to 10^{-4} arcsec, making at present impossible the eventual observation of the CS fractal structure.

$\Delta\lambda_{\text{eff}}$ of a spectral line emitted from ions with mass m_i at a kinetic temperature T_i is given by

$$\Delta\lambda_{\text{eff}} = 2\sqrt{\ln 2} \frac{\lambda_0}{c} \sqrt{\frac{2k_B T_i}{m_i} + v_{\text{Nth}}^2}, \quad (2)$$

where λ_0 is the position of the line centroid, c is the speed of light, and k_B is the Boltzmann constant. This equation can be used to estimate v_{Nth} , once $\Delta\lambda_{\text{eff}}$ and T_i are known. However, in general, not only v_{Nth} , but also T_i is unknown, and it is impossible to derive both parameters simply from the observed line profile width.

A possible solution to the problem exists if one can assume that the plasma is isothermal, so that $T_i \approx T_e$, where T_e is the electron temperature. Usually, electron temperature T_e is derived from UVCS spectra using the line-ratio technique, i.e., from the intensity ratios of lines from different ions of the same element, under the assumption that they originate in the same isothermal plasma. In order to verify the validity of the assumption that $T_i \approx T_e$, we can estimate the time τ_{eq} required for the equipartition of energy by collisions between protons and ions emitting the observed spectral line and between protons and electrons. If we consider in a fully ionized gas, the collisions occurring between test particles 1 (with charge Z_1 , atomic mass number A_1 , and temperature T_1) and field particles 2 (with charge Z_2 , atomic mass number A_2 , temperature T_2 , and number density n_2), the time for energy equipartition is

$$\tau_{\text{eq}} = (5.87) \frac{A_1 A_2}{n_2 Z_1^2 Z_2^2 \ln \Lambda} \left(\frac{T_1}{A_1} + \frac{T_2}{A_2} \right)^{3/2} \quad (3)$$

(Spitzer 1962), where $\ln \Lambda = \ln (8.0 \times 10^6 T_e n_e^{-1/2})$ is the Coulomb logarithm (with the electron density n_e in cm^{-3}). This time has to be much smaller than the heating timescale of plasma flowing toward the CS; an order of magnitude estimate for this time is given by the time $\tau_{\text{cross}} = D/v_{\text{in}}$ required to the coronal plasma, flowing with velocity v_{in} toward the CS, to cross the CS thickness D . If $\tau_{\text{eq}} \ll \tau_{\text{cross}}$ holds in the specific event, we can estimate v_{Nth} by taking $T_i = T_e$ in equation (2).

Before doing so, another effect needs to be considered that may cause extra broadening of spectral line profiles. The observed width $\Delta\lambda_{\text{obs}}$ is, in general, larger than the effective width $\Delta\lambda_{\text{eff}}$ because the observed profile is a convolution between the line emission profile and the instrumental profile that results in a broadening of the observed spectral line. The correction for this effect is quite complex because it involves the deconvolution of the observed profile with an instrumental profile that, being unknown, needs to be simulated. This work uses the empirical formula given by Kohl et al. (1999) that expresses the FWHM correction $\Delta\lambda_{\text{corr}}$ (in units of pixels) for the UVCS line profile broadening as

$$\Delta\lambda_{\text{corr}} = \sqrt{(\Delta\lambda_{\text{iw}})^2 + \frac{2}{3} \ln 2 \left[P^2 + \left(\frac{W}{0.025 \text{ mm}} \right)^2 \right]}, \quad (4)$$

where $\Delta\lambda_{\text{iw}}$ is the instrumental line width, P is the number of pixels per bin, and W is the slit width in millimeters. The $\Delta\lambda_{\text{corr}}$ has to be subtracted in quadrature from the width $\Delta\lambda_{\text{obs}}$ obtained by the line profile fitting, so that the effective FWHM is $\Delta\lambda_{\text{eff}} = (\Delta\lambda_{\text{obs}}^2 - \Delta\lambda_{\text{corr}}^2)^{1/2}$.

Once the profile has been corrected for instrumental effect and the v_{Nth} has been estimated, it is necessary to discuss the physical origin of nonthermal motions. A spectral line broadening can be

due to motions of the emitting plasma occurring with a velocity component projected along the line of sight in both directions, i.e., away and toward the observer. Nonthermal broadenings observed by UVCS have been ascribed, for instance, to the expansion of CME fronts (see, e.g., Bemporad et al. 2006; Ciaravella et al. 2006) and to turbulent motions occurring in post-CME CSs (Ciaravella et al. 2002; Ciaravella & Raymond 2008), while line broadenings observed in fast solar wind have been ascribed to the preferential heating of heavy ions occurring in coronal holes (see Kohl et al. 2006 and references therein). In general, the existence and eventual contributions from these effects to the observed line profile width has to be discussed in each observation data set.

3. EVOLUTION OF TURBULENCE IN CSs FROM [Fe xviii] PROFILES

In the wavelength range covered by UVCS, the most suitable spectral line for the study of nonthermal motions in post-CME CSs is the [Fe xviii] $\lambda 974.8$ line. As mentioned in § 1, the emissivity of this line peaks at a very high temperature of maximum formation; hence, information derived from the observed line width characterizes only the ‘‘hot’’ CS plasma, because in the integration along the line of sight coronal plasma give no contribution to the observed [Fe xviii] profile. Although typical spectral binning of UVCS observations is between ~ 0.2 and ~ 0.3 Å (hence between $\simeq 60$ and $\simeq 90$ km s^{-1} for $\lambda_0 = 974.8$ Å) the detection of nonthermal line broadening due to turbulent motions even with small velocities is possible. For instance, by assuming a typical CS temperature $T_e \simeq 4 \times 10^6$ K and $T_i = T_e$, equation (2) gives $\Delta\lambda_{\text{eff}} \simeq 0.19$ Å for $v_{\text{Nth}} = 0$ km s^{-1} and $\Delta\lambda_{\text{eff}} \simeq 0.33$ Å for $v_{\text{Nth}} = 50$ km s^{-1} . With $\Delta\lambda_{\text{corr}} \sim 0.3$ Å, these widths should be observed as $\Delta\lambda_{\text{obs}} \simeq 0.35$ and 0.45 Å, respectively. This difference by ~ 0.1 Å in the profile FWHM can be inferred with standard Gaussian fits for data sets where the [Fe xviii] line has been observed for at least a few hours, making it possible to derive average line profiles with a very large number of counts (e.g., $\approx 10^3$ counts at the line peak) and hence very good statistics (e.g., $\Delta n/n = 1/\sqrt{n} \approx 2\% - 3\%$). The following two sections describe the Fe xviii kinetic temperatures derived in all the CSs observed by UVCS and reported so far (§ 3.1) and then concentrate on the evolution of nonthermal velocities in the 2002 November (Paper I) event (§ 3.2).

3.1. Fe xviii Kinetic Temperatures in CSs

As mentioned above, observations of the [Fe xviii] line in post-CME CSs reported so far (Ciaravella et al. 2002; Ko et al. 2003; Raymond et al. 2003; Bemporad et al. 2006; Lee et al. 2006; Ciaravella & Raymond 2008) show a strong line emission, but observational periods typically do not exceed a few hours, making it difficult to perform a complete study on the evolution of the line profile from each single data set. The only UVCS data set published so far in which the [Fe xviii] line has been observed continuously for days after the CME is the one we reported in Paper I; these unique observations covered a period of ~ 2.3 days (starting ~ 1.5 hr after the CME) and were characterized by a strong [Fe xviii] emission detected during the whole time interval over a broad spatial region covering approximately $\sim 7'$ along the spectrometer slit (see Paper I, Figs. 5 and 6). However, previous CS observations of the [Fe xviii] spectral line detected this high-temperature emission in just the first few hours after the CME because of the short duration of observations (Ciaravella et al. 2002) or because \sim hours after the eruption [Fe xviii] emission disappears. Only in the event reported by Ko et al. (2003) was [Fe xviii] emission observed for ~ 6 hr, starting from ~ 2.1 days

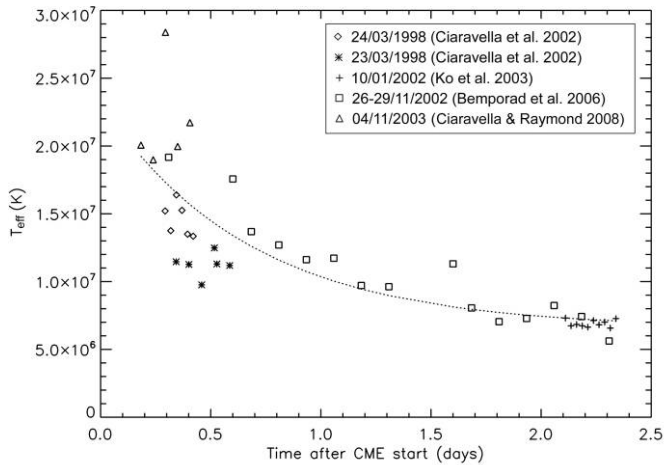


FIG. 3.— Evolution with time of [Fe xviii] effective kinetic temperatures T_{eff} for different post-CME CSs observed by UVCS in this line and reported so far. For each event T_{eff} values are plotted as a function of time measured starting from the occurrence of the CME related to each CS; the dotted line shows the exponential decay fitting function (see text).

after the related eruption. This means that an analysis of [Fe xviii] profiles in the first hours after the CME from data sets reported by Ciaravella et al. (2002), Raymond et al. (2003), Bemporad et al. (2006), Lee et al. (2006), and Ciaravella & Raymond (2008), and more than 2 days after the eruption from data sets reported by Ko et al. (2003) and Bemporad et al. (2006), may give, in principle, a complete picture on the evolution of plasma turbulence in CSs.

Hence, this work studies [Fe xviii] line profiles in all of the already published events where this line has been observed in a CS, with the exception of data reported by Raymond et al. (2003) and Lee et al. (2006) for the event of 2002 April 21, whose very short duration (≤ 15 minutes) of [Fe xviii] emission is not suitable for a study of line profiles. Different events have been observed with the spectrometer slit centered at heliocentric distances ranging between 1.5 and 1.7 R_{\odot} using different combinations of observational parameters, such as different spatial binnings (42'' or 70''), exposure times (120 or 200 s), and slit widths (50 or 100 μm). Hence, in order to compare [Fe xviii] line widths measured in various events, the observed spectra have been averaged over the number of spatial bins and exposures needed to have $\approx 10^3$ counts at the line peak in each profile. The [Fe xviii] profile FWHMs have been computed with a standard Gaussian fit; the resulting effective kinetic temperatures T_{eff} (i.e., due to ion kinetic temperature T_i , turbulence or other plasma motions; see eq. [2]) corrected for the instrumental line broadening (eq. [4]) are shown in Figure 3. Values given in Figure 3 have been computed as

$$T_{\text{eff}} = \frac{1}{4 \log 2} \frac{m_i c^2}{2k_B} \left(\frac{\Delta \lambda_{\text{eff}}}{\lambda_0} \right)^2. \quad (5)$$

In the hypothesis that the effective kinetic temperatures T_{eff} measured in different events refer to different stages during the CS lifetime and in order to increase the significance of this comparison, T_{eff} values are plotted in Figure 3 as a function of days from the estimated starting time of the CME related to each CS.⁶ This

⁶ For the event reported by Ciaravella & Raymond (2008) all data points higher than $\sim 3 \times 10^7$ K have been excluded, because the authors ascribed these higher temperatures to pre-CME corona and flare emission and to the transit of plasmoids along the CS (see Ciaravella & Raymond 2008, Fig. 9, and related discussion).

figure shows that differences in T_{eff} values measured for various events are larger in the first few hours after the CME; a comparison between mass, velocity, flare association, etc., of all the involved eruptions gives any apparent difference between the events with highest and lowest T_{eff} values. In any case, Figure 3 shows a general trend; values measured for the 2002 November 26–29 CS (reported in Paper I) are in good agreement with those measured for the Ko et al. (2003) event ~ 2.1 days after the CME and in quite good agreement with those measured for the Ciaravella et al. (2002) and Ciaravella & Raymond (2008) events a few hours after the CME. The [Fe xviii] effective kinetic temperatures are $\sim 2 \times 10^7$ K about 5–6 hr after the CME and decrease slowly in the following 2 days down to a final value of $\sim (6-7) \times 10^6$ K. The T_{eff} values reported in Figure 3 are much larger than the CS electron temperatures that are on the order of $\sim (8-6) \times 10^6$ a few hours after the CME (Ciaravella et al. 2002; Bemporad et al. 2006; Ciaravella & Raymond 2008) and decrease down to $\sim (3-4) \times 10^6$ after ~ 2 days (Ko et al. 2003; Bemporad et al. 2006). This indicates that significant nonthermal line broadening is present in the observed emission. By fitting all data points shown in Figure 3 with an exponential function of the form $y = y_0 + A \exp(-t/\tau)$, it turns out that $y_0 = 6.6 \times 10^6$ K, $A = 1.7 \times 10^7$ K, and $\tau = 0.67$ days, which corresponds to a half-life of $t_{1/2} = \tau \ln 2 = 0.47$ days.

Because of the quite good agreement shown in Figure 3 between T_{eff} values for the event reported in Paper I and those measured for other events, and because the 2002 November CS is the only one observed for more than 2 days, the following analysis concentrates on the evolution of turbulence in this event. As shown in Figure 3, even if physical parameters derived in the following sections are relative only to this event, these can be considered as representative of a general behavior of post-CME CSs. The 2002 November 26–29 observations have also the advantage that, as concluded from the position and orientation of the post-CME loops (see Paper I, Fig. 2, and related discussion), the CS was observed approximately face-on, lying on the plane of the sky, while in other observations reported so far the CS was aligned with the line of sight and hence was seen edge-on. The face-on geometry has the advantage that the effect of line broadening related to plasma diverging flows along the CS is minimized,⁷ while for a fan-shaped CS seen edge-on a contribution of flows to the line width cannot, in principle, be excluded (see discussion in Ciaravella & Raymond 2008). For this reason, line broadening due to flows occurring along the CS can be excluded, and in the following analysis the observed nonthermal [Fe xviii] line broadening is ascribed entirely to turbulent motions occurring with velocity v_{turb} in the CS plasma, also in agreement with the interpretation given by Ciaravella et al. (2002) and Ciaravella & Raymond (2008).

3.2. Turbulent Motions in the 2002 November CS

The 2002 November observations were acquired with a time resolution of 120 s (with ~ 10 s gaps between two successive exposures) in various data sets including 72–80 exposures each. In order to study the evolution of [Fe xviii] line profiles, each data set has been averaged over all exposures; each single profile studied here represents an average over $\sim 2.6-2.9$ hr of data. Line profiles have also been averaged over a 3 spatial bins interval

⁷ At a heliocentric distance of 1.7 R_{\odot} the line-of-sight component v_{LOS} of outflows for a CS seen face-on, on the order of $\sim 3\%$ and $\sim 0.1\%$ of the outflow velocity for a diffusion region located, respectively, at 1.1 and 1.5 R_{\odot} (B. Vršnak 2008, private communication).

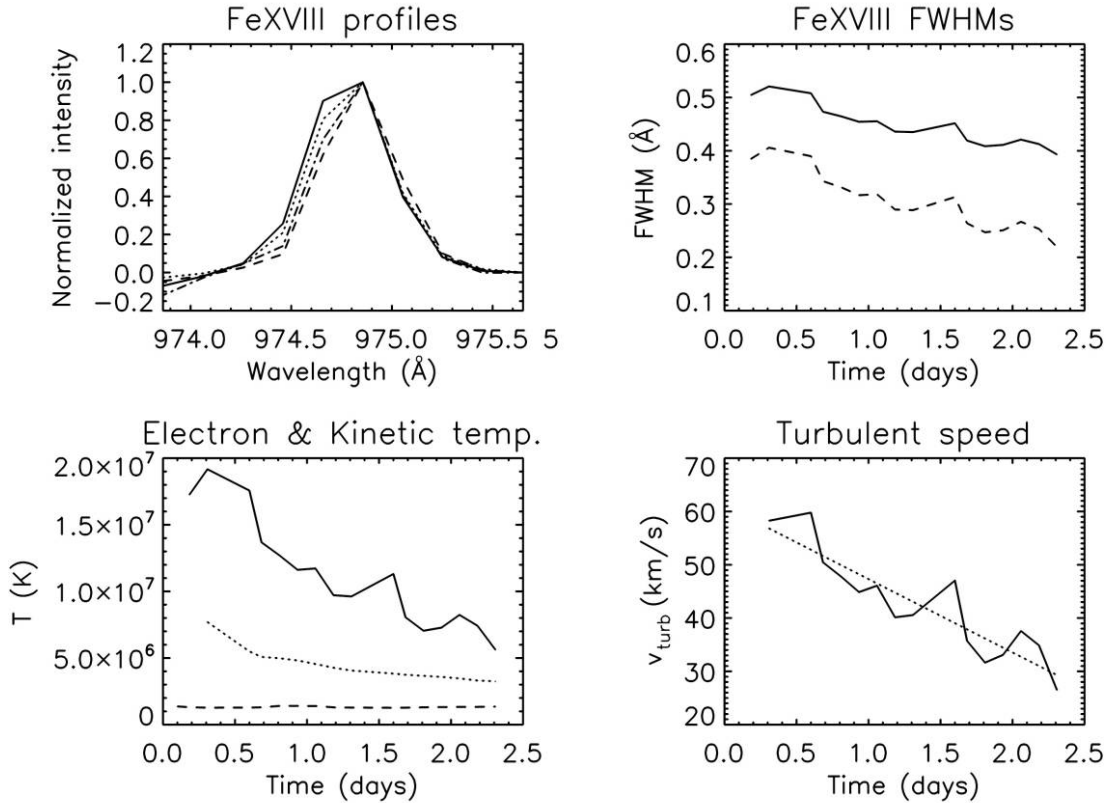


FIG. 4.— *Top left*: [Fe xviii] normalized line profiles 0.18 (*solid line*), 0.68 (*dotted line*), 1.18 (*dash-dotted line*) and 2.3 days after the CME. On average, Poissonian uncertainties are on the order of $\sim 2\%$ – 3% at the peak and $\sim 4\%$ – 5% at $1/e$ of the peak for each profile. *Top right*: Evolution of FWHMs from Gaussian fits (*solid line*) and FWHMs after correction for the instrumental line broadening (*dashed line*). *Bottom left*: Derived evolution of the Fe xviii effective kinetic temperatures T_{eff} (*solid line*) and electron temperatures T_e inside the CS (*dotted line*) and in the outer corona (*dashed line*). *Bottom right*: Observed evolution of turbulent velocity (*solid line*) and the linear fit to the curve (*dotted line*).

(i.e., $2.1'$) along the slit centered at the latitude where [Fe xviii] emission maximizes. A comparison between average normalized [Fe xviii] profiles at different times (Fig. 4, *top left panel*) shows a progressive decrease in the observed line width during the ~ 2.3 days after the CME. Results from a standard Gaussian fit show that $\Delta\lambda_{\text{obs}}$ decreases by ~ 0.1 Å from ~ 0.5 to ~ 0.4 Å (Fig. 4, *top right panel*). The [Fe xviii] profiles were acquired with a spectral binning of 2 pixels (~ 0.2 Å) and hence larger than the observed FWHM decrease; however, thanks to the very large number of counts available for each profile, Poissonian uncertainties are on the order of $\sim 2\%$ – 3% at the peak and $\sim 4\%$ – 5% at $1/e$ of the peak. This implies that differences in [Fe xviii] profiles shown in Figure 4 are larger than actual uncertainties.

The effective kinetic temperature T_{eff} (computed from the $\Delta\lambda_{\text{obs}}$ values corrected for instrumental line broadening; see eq. [4]) decreases from $\sim 1.8 \times 10^7$ K down to $\sim 6 \times 10^6$ K (Fig. 4, *bottom left panel*). A comparison between the T_{eff} curve (*solid line*) and the electron temperature T_e evolution (*dotted line*) derived in Paper I from the line ratio technique⁸ shows that [Fe xviii] line profiles are nonthermally broadened ($T_{\text{eff}} > T_e$). As discussed above, thanks to the CS face-on view, contribution to this broadening from out- and in-flow pairs occurring along the CS are

minima and can be mainly ascribed to plasma turbulence. However, Figure 4 (*top left panel*) shows a clear asymmetry in the narrowing of the [Fe xviii] line profiles that occurs mostly in the line blue wing and corresponds to a line Doppler shift by ~ 0.1 Å toward longer wavelengths during the ~ 2 days of observations. This blue to red shift is probably related to outward plasma bulk motions occurring along the CS; during the observations (performed above the west limb; see Paper I, Figs. 2 and 3) the CS structure is dragged by the solar rotation behind the plane of the sky, changing the projection of outflow speed along the line of sight and leading to the observed line shift.

From the observed T_{eff} values, turbulent velocities v_{turb} have been computed by assuming $T_i = T_e$ as

$$v_{\text{turb}} = \sqrt{\frac{2k_B}{m_{\text{Fe}}}(T_{\text{eff}} - T_e)}. \quad (6)$$

The resulting v_{turb} values as a function of time are shown in Figure 4 (*bottom right panel*); these curves show that nonthermal broadening corresponds to an average turbulent velocity $v_{\text{turb}} \approx 45$ km s⁻¹ and that v_{turb} decreases with time from ~ 60 km s⁻¹ down to ~ 30 km s⁻¹. A linear fit of the v_{turb} versus t curve gives a deceleration of turbulent motions $\Delta v_{\text{turb}}/\Delta t = (0.17 \pm 0.2)$ m s⁻²; implications from these results are discussed in the next sections.

As discussed (§ 2), the assumption that $T_i = T_e$ needs to be justified by estimating the equipartition times (eq. [3]) and CS crossing time; by assuming that in the external corona $T_2 = 1 \times 10^6$ K,

⁸ Electron temperatures in the CS $T_e(\text{CS})$ have been derived using the ratio between the observed intensities of [Fe xviii] $\lambda 974.8$ and Fe xv $\lambda 481.5$ spectral lines, while for coronal temperatures $T_e(\text{COR})$ we resort to the ratio between [Si viii] $\lambda 944$ and [Si ix] $\lambda 950$ lines. Resulting CS and coronal temperatures are shown in the bottom left panel of Fig. 4 (see Paper I for a description of the electron temperature computational methods).

$n_2 = 1 \times 10^7 \text{ cm}^{-3}$, and that the plasma is out of thermal equilibrium with $T_1 = 10 T_2$, the equipartition times turn out to be $\tau_{\text{eq}}(e^- e^-) \sim 23 \text{ s}$, $\tau_{\text{eq}}(p^+ p^+) \sim 990 \text{ s}$, and $\tau_{\text{eq}}(p^+ e^-) \sim 1200 \text{ s}$, respectively, for self-collisions among protons, electrons, and collisions among protons and electrons. Hence, electrons come to a thermal equilibrium more rapidly than protons, and finally equipartition between electron and protons is established. As mentioned above, these times have to be compared with the time τ_{cross} required to the coronal plasma, flowing with velocity V_{in} toward the CS, to cross the CS thickness D . By assuming for instance $V_{\text{in}} \sim 10 \text{ km s}^{-1}$ and $D \sim 10^4 \text{ km}$, it turns out that $\tau_{\text{cross}} \sim 10^3 \text{ s} \sim \tau_{\text{eq}}(p^+ p^+) \sim \tau_{\text{eq}}(p^+ e^-)$; hence, the condition for the energy equipartition that $\tau_{\text{eq}} \ll \tau_{\text{cross}}$ is not fulfilled.⁹ However, the near equality between τ_{eq} and τ_{cross} suggests that we are not very far from the energy equipartition. In conclusion, the assumption made here that $T_i = T_e$ may correspond to an underestimate for T_i , and in the following the v_{turb} values derived with equation (6) have to be considered as an upper limit estimate to real turbulent velocities.

4. PHYSICAL CURRENT SHEET PARAMETERS AT MACROSCOPIC LEVEL

Starting from the turbulent velocity evolution described above, it is possible to derive additional information on the plasma physical parameters in the CS. To this end, in the following the electron density n_e and temperature T_e derived in Paper I for the CS and external coronal plasmas (see Paper I, Figs. 11 and 13) are used as a computation starting point. As a working hypothesis, the CS plasma parameters derived in Paper I are considered as representative of plasma in a broad region (namely, macroscopic CS [MCS]) where, due to the presence of turbulence, reconnections occur locally in much smaller regions (namely, microscopic CS [μCS]); this assumption and its implications will be discussed in greater detail in the following sections. Magnetic reconnections occurring in the MCS result in ohmic heating and plasma acceleration and dissipate magnetic energy density u_m (J m^{-3}), converting it into thermal (ϵ_t) and kinetic energy densities (ϵ_k). From the energy conservation we can write that

$$u_m(\text{MCS}) = [\epsilon_k(\text{MCS}) - \epsilon_k(\text{COR})] + [\epsilon_t(\text{MCS}) - \epsilon_t(\text{COR})], \quad (7)$$

where $u_m(\text{MCS})$ is the magnetic energy density of the MCS “ambient” plasma being reconnected locally in μCS s, $\epsilon_k(\text{MCS})$ and $\epsilon_k(\text{COR})$ are the MCS plasma kinetic energy density (including turbulence motions) and the coronal plasma kinetic energy density (due to inflow motions), respectively, and $\epsilon_t(\text{MCS})$ and $\epsilon_t(\text{COR})$ are the MCS and external coronal plasma thermal energies, respectively. However, the above equation is not correct, because the thermal energy increase $\Delta\epsilon_t = \epsilon_t(\text{MCS}) - \epsilon_t(\text{COR})$ is provided not only by magnetic reconnection, but also by the adiabatic compression that coronal plasma undergoes flowing into the MCS. Taking also into account adiabatic heating and defining f and $(1-f)$ as the fractions of magnetic energy that go into thermal and kinetic energies, respectively, equation (7)

⁹ The conclusion that $\tau_{\text{eq}} \sim \tau_{\text{cross}}$ is not in contradiction with the usual assumption that the coronal plasma is a collisionless environment: Depending on the local coronal plasma physical conditions typically above $\sim 2-3 R_{\odot}$, the characteristic time for coronal expansion τ_{exp} is smaller than thermalization times τ_{eq} , making the plasma out of thermal equilibrium, while below this altitude is $\tau_{\text{exp}} > \tau_{\text{eq}}$ and thermal equilibrium is usually assumed (see Withbroe et al. 1982).

can be rewritten and divided in two equations as follows (MKS units):

$$f \frac{B^2(\text{MCS})}{2\mu_0} = 3k_B [n_e(\text{MCS})T_e(\text{MCS}) - n_e(\text{COR})T_e(\text{COR})] - 3k_B T_e(\text{COR})n_e(\text{COR}) \left\{ \left[\frac{n_e(\text{MCS})}{n_e(\text{COR})} \right]^\gamma - 1 \right\}, \quad (8)$$

$$(1-f) \frac{B^2(\text{MCS})}{2\mu_0} = \frac{1}{2} \rho(\text{MCS})(v_{\text{flow}}^2 + v_{\text{turb}}^2) - \frac{1}{2} \rho(\text{COR})(v_{\text{wind}}^2 + V_{\text{in}}^2), \quad (9)$$

where $\gamma = 5/3$, $\Delta\epsilon_\gamma = 3k_B T_e(\text{COR})n_e(\text{COR}) \{ [n_e(\text{MCS})/n_e(\text{COR})]^\gamma - 1 \}$ is the thermal energy increase due solely to the adiabatic compression, and $B(\text{MCS})$ is the “ambient” magnetic field in the MCS. In the above equations it has been assumed that the plasma “macroscopic” kinetic energy inside the MCS results from a superposition of turbulent motions and bulk translation flows (i.e., inflows and outflows) occurring inside the MCS region with average velocities v_{turb} and v_{flow} , respectively, while in the external corona the kinetic energy results from a superposition of solar wind speed and inflow toward the MCS, occurring with average velocities v_{wind} and V_{in} , respectively. Given f and the plasma physical parameters (n_e , T_e) inside and outside the MCS, equation (8) contains only an unknown quantity, the MCS ambient magnetic field B , that can be estimated. Usually, for plasmas with low values of $\beta = p_{\text{gas}}/p_{\text{mag}}$ [where $p_{\text{gas}} = 2n_e k_B T_e$ is the thermal plasma pressure and $p_{\text{mag}} = B^2/(2\mu_0)$ is the magnetic pressure], it is assumed that energy equipartition holds, so that $f = 1/2$. However, both laboratory plasma experiments (see, e.g., Hsu et al. 2000) and simulations (see, e.g., Karlický & Bárta 2008) suggest that during magnetic reconnection a larger fraction of magnetic energy goes into ion kinetic energy. As a consequence, in the following computation it has been assumed that $f = 2/5$ (see Ji et al. 2004), constant with time.

From equation (9) it turns out that the inflow/outflow speed v_{flow} along the MCS is given by

$$v_{\text{flow}} = \left[\frac{\rho(\text{COR})}{\rho(\text{MCS})} (v_{\text{wind}}^2 + V_{\text{in}}^2) + \frac{(1-f)B^2(\text{MCS})}{\mu_0 \rho(\text{MCS})} - v_{\text{turb}}^2 \right]^{1/2}. \quad (10)$$

In this equation the only unknown quantities are the external corona wind speed v_{wind} and the inflow speed V_{in} toward the MCS. In the computation it has been assumed at $1.7 R_{\odot}$ that $v_{\text{wind}} \simeq 130 \text{ km s}^{-1}$ (see Kohl et al. 2006, Fig. 41) and $V_{\text{in}} \simeq 10 \text{ km s}^{-1}$ (see Lin et al. 2007 and references therein). Note that in equation (10) these two velocities are both multiplied by a factor $\rho(\text{COR})/\rho(\text{MCS}) \sim 0.16$ in our case;¹⁰ hence, the results for v_{flow} do not depend strongly on values assumed for v_{wind} and V_{in} .

¹⁰ Note that for plasmas with $\beta \ll 1$ the jump in plasma density $x = \rho(\text{MCS})/\rho(\text{COR}) \simeq 6.2$ should be $1 < x < 4$. However, the MCS density at a fixed altitude is due not only to the compression of external coronal plasma located at the same altitude, but also (and possibly for a larger fraction) to the plasma flowing along the MCS from the underlying levels. The latter is a much denser plasma because it comes from the compression of coronal plasma located at lower levels, leading to the observed larger compression ratio x .

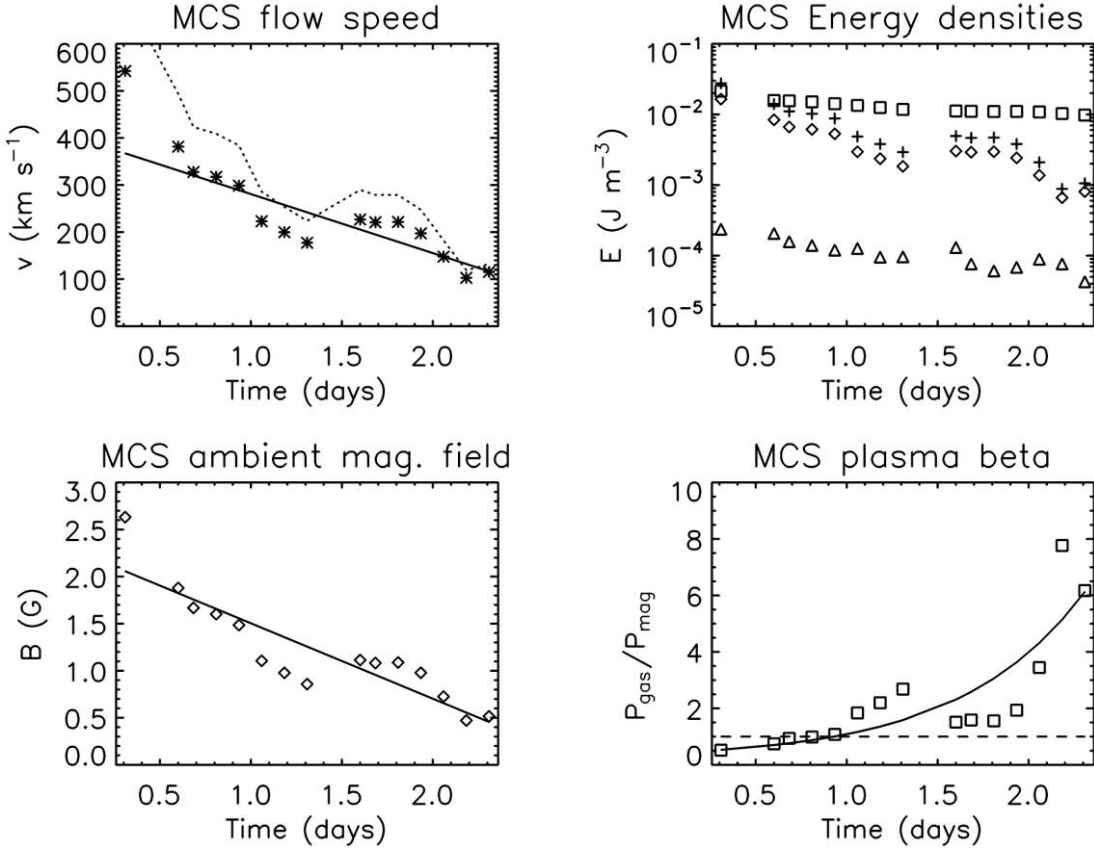


FIG. 5.— *Top left:* Evolution of flow velocity along the MCS (asterisks), the linear fit to data (solid line), and the Alfvén velocity (dotted line). *Top right:* Evolution of thermal energy density (squares), magnetic energy density (plus signs), and densities of kinetic energy related to turbulence (triangles) and flow along the MCS (diamonds). *Bottom left:* evolution of the MCS ambient magnetic field (diamonds) and the linear fit to data (solid line). *Bottom right:* evolution of MCS plasma β (squares) and the exponential fit to data (solid line).

The values derived for the MCS flow speed v_{flow} (from eq. [10]), MCS magnetic field $B(\text{MCS})$ (from eq. [8] with $f = 2/5$), kinetic, thermal, and magnetic energy densities, and the plasma β are all given in Figure 5 as a function of time. This figure shows that the ambient magnetic field is on the order of a few Gauss, decreasing with time from ~ 2 to ~ 0.5 G; thermal and kinetic energies are also decreasing at approximately the same rate, while the magnetic energy is decreasing at a larger rate. Hence, the resulting MCS plasma beta is $\beta < 1$ only at the beginning of our observations, while later on, because of the faster decrease in the magnetic pressure, β increases up to $\beta \sim 5$. The magnetic field decrease toward a final value close to 0 shown in Figure 5 is in good agreement with the conclusion given in Paper I that at the end of our observations the adiabatic compression can account for the MCS plasma heating (Paper I, Fig. 17). Given the ambient magnetic field B and electron density n_e , the Alfvén speed v_A can also be estimated; Figure 5 (*top left panel*) shows that $v_{\text{flow}} \lesssim v_A$, as expected, and that on average $v_{\text{flow}} \simeq v_A \simeq 300 \text{ km s}^{-1}$. Values given in Figure 5 for B and v_A will be used in the following computations.

5. ESTIMATE OF LOCAL ANOMALOUS DIFFUSIVITY

The purpose of this section is to use the MCS plasma parameters derived in the previous sections in order to estimate the localized nonclassical diffusivity due to microscopic instabilities. As a first step, it is possible to compute from the observed w_{turb} values the relative turbulent energy density w_{turb} that is a measure of the turbulent energy density $\epsilon_k(\text{turb}) = \frac{1}{2} n_e(\text{MCS}) m_p v_{\text{turb}}^2$

compared to the thermal energy density inside the MCS and is given by

$$w_{\text{turb}} = \frac{\epsilon_k(\text{turb})}{\epsilon_t(\text{MCS})} = \frac{m_p v_{\text{turb}}^2}{4k_B T_e(\text{MCS})}. \quad (11)$$

It turns out that $w_{\text{turb}} \simeq 1.2\%$ at the beginning of our observations and decreases down to $w_{\text{turb}} \simeq 0.6\%$ in the following days (see Fig. 5, *top right panel*). From the theoretical point of view, there are many physical processes that can produce turbulence by microscopic plasma instabilities. However, in a reconnecting plasma where the current densities are expected to be large due to the strong magnetic field gradients at the reconnection sites, the main role will be played by current-aligned instabilities (e.g., Norman & Smith 1978) and, hence, instabilities able to generate collisionless waves propagating mainly parallel to the direction of currents. Such waves induce additional alternating or fluctuating electric fields $\mathbf{E}' = \mathbf{E} + \mathbf{v} \times \mathbf{B}$ that, interacting with currents \mathbf{j} , are able to provide additional dissipation $\mathbf{j} \cdot \mathbf{E}' \neq 0$, resulting in an enhanced plasma diffusivity η^* (namely, anomalous diffusivity or anomalous resistivity), much higher than the classical one (see Büchner 2007 for a recent review). The main candidate microscopic plasma instabilities able to generate anomalous diffusivity in CSs are the ion-acoustic (IA) and lower hybrid drift (LHD) instabilities. In the following I investigate both these processes, and I derive from the observed turbulent energy density an estimate for the corresponding anomalous diffusivities.

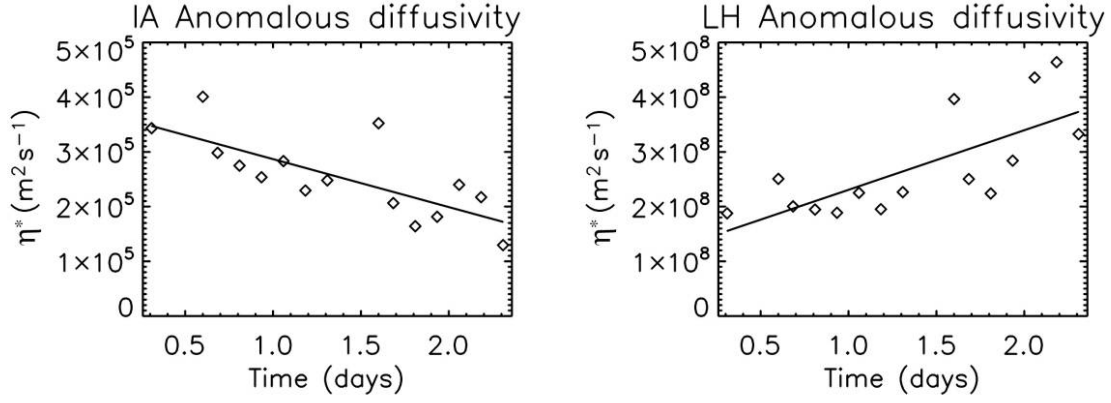


FIG. 6.— Evolution of anomalous diffusivities η^* as computed from the observed turbulent velocities v_{turb} (Fig. 4) in the hypothesis of ion-acoustic (*left*) or lower hybrid drift (*right*) instabilities.

5.1. Ion-Acoustic Instability

The IA instability is excited by the resonant interaction of drifting electrons or ions with the electric field oscillations of ion-acoustic waves. In astrophysical plasmas the IA instabilities are important only when $T_e \gg T_i$ (see Smith & Priest 1972); hence, this instability is usually ineffective in the almost isothermal solar corona. However, for strong driven currents (as it happens in CSs) this instability may develop even in plasmas with $T_e \approx T_i$ (see Birn & Priest 2007, pp. 145–146, and references therein). Recent simulations concluded that the IA instability could be an important process in reconnecting CSs (Wu et al. 2005; Büchner & Elkina 2006; Karlický & Barta 2008) and revived the interest in this instability. In the case $T_e \approx T_i$ the IA instability is excited if the drift velocity $v_d = |v_{i\parallel} - v_{e\parallel}|$ (where $v_{i\parallel}$ and $v_{e\parallel}$ are the ion and electron velocities parallel to the electric currents, respectively) is larger than the critical value $v_{d,\text{crit}}$ given by the electron thermal speed $v_e^{\text{th}} = (k_B T_e / m_e)^{1/2}$ (Smith & Priest 1972). This critical drift velocity corresponds to a critical current $j_{\text{crit}} = n_e e v_{d,\text{crit}}$ and hence to a critical CS thickness d_{crit} on the order of

$$d_{\text{crit}} \sim \frac{B}{\mu_0 j_{\text{crit}}}. \quad (12)$$

In our MCS, assuming a magnetic field $B \sim 1$ G (see Fig. 5), $T_e \sim 4 \times 10^6$ K, and $n_e \sim 7 \times 10^{13} \text{ m}^{-3}$, it turns out that $d_{\text{crit}} \approx 1$ m. This quite stringent condition can be satisfied only if turbulent reconnection occurring at microscopic levels is envisaged. If we hypothesize that IA instability is responsible for the observed turbulent motions, given the fraction w_{turb} of turbulent energy density the corresponding anomalous diffusivity η_{IA}^* ($\text{m}^2 \text{s}^{-1}$) is given by

$$\eta_{\text{IA}}^* = \frac{m_e}{\mu_0 n_e e^2 \tau_{\text{IA}}^*} = \frac{m_e \omega_{\text{pe}}}{\mu_0 n_e e^2} w_{\text{turb}} \quad (13)$$

(Priest 1982, pp. 79–80), where $\tau_{\text{IA}}^* \approx 1/(w_{\text{turb}} \omega_{\text{pe}})$ is the IA anomalous collision time and $\omega_{\text{pe}} \approx 9.0(n_e)^{1/2} \text{ s}^{-1}$ is the electron plasma frequency if n_e is in m^{-3} . With $n_e \sim 7 \times 10^{13} \text{ m}^{-3}$ and $w_{\text{turb}} \sim 0.01$, it turns out that $\eta_{\text{IA}}^* \approx 3 \times 10^5 \text{ m}^2 \text{ s}^{-1}$, in agreement with values found by previous authors (see, e.g., Lin et al. 2007). Values for η_{IA}^* computed at different times are shown in Figure 6 (*left panel*). Consequences of these values and on the evolution with time of η_{IA}^* will be discussed in § 7.

5.2. Lower Hybrid Drift Instability

The LHD instability is driven by drifts associated with strong pressure gradients; the “advantage” with respect to the IA instability is that LHD waves are excited even for plasmas with $T_e < T_i$ (see Davidson & Gladd 1975). However, the theory predicts that the fastest growing modes are localized at the edge of the current layer and that in the central region significant anomalous diffusivity is hardly produced (see Birn & Priest 2007, pp. 145–146, and references therein). Recent simulations showed that longer wavelength LHD modes can penetrate into the central region of the current layer increasing the diffusivity (see, e.g., Daughton 2003; Silin & Büchner 2003; Daughton et al. 2004; Ricci et al. 2005), and the magnetic fluctuations in the LHD frequency range have been observed during reconnection in laboratory plasma (e.g., Ji et al. 2004); these results gave to the LHD instability a “new role” in the magnetic reconnection theory. The LHD instability is more easily excited than the IA instability because the required critical CS thickness is on the order of

$$d_{\text{crit}} = \frac{B}{\mu_0 j_{\text{crit}}} = \frac{B}{\mu_0 n_e e} \sqrt{\frac{m_i}{k_B T_i}} \quad (14)$$

that, assuming $T_i \sim T_e \sim 4 \times 10^6$ K and numbers given above, is on the order of ~ 40 m. As pointed out by Kulsrud (2001), this thickness has to be compared with the classical Sweet & Parker thickness $\delta_{\text{SP}} = (2L\eta/v_A)^{1/2}$. For a Sweet & Parker CS length $L \sim 1 R_\odot \sim 7 \times 10^5$ km and assuming an Alfvén speed $v_A \sim 10^3 \text{ km s}^{-1}$ it turns out that $\delta_{\text{SP}} \sim 40 \text{ m} \sim d_{\text{crit}}$; hence, the LHD instability should be excited if small-scale reconnection is occurring. If the observed fraction of turbulent energy density w_{turb} is ascribed to LHD instability [so that $w_{\text{turb}} = \epsilon_0 \delta E^2 / (2nk_B T_e)$, where $\epsilon_0 \delta E^2$ is the wave energy density associated with electric field fluctuations δE] the corresponding anomalous diffusivity η_{LH}^* ($\text{m}^2 \text{s}^{-1}$) is given by

$$\eta_{\text{LH}}^* = \frac{m_e}{\mu_0 n_e e^2 \tau_{\text{LH}}^*} = \frac{m_e \omega_{\text{pe}}}{\mu_0 n_e e^2} \frac{\omega_{\text{pe}}}{\Omega_{\text{LH}}} w_{\text{turb}} \quad (15)$$

(see Büchner 2007), where $\tau_{\text{LH}}^* \approx \Omega_{\text{LH}} / (w_{\text{turb}} \omega_{\text{pe}}^2)$ is the LHD anomalous collision time, $\Omega_{\text{LH}} = \omega_{\text{pi}} / (1 + \omega_{\text{pe}}^2 / \Omega_e^2)^{1/2}$ is the LHD frequency (see Huba et al. 1977), $\omega_{\text{pi}} \approx 0.21(n_e)^{1/2} \text{ s}^{-1}$ is the ion (proton) plasma frequency (with n_e in m^{-3}), and $\Omega_e = eB/m_e \sim 2.8 \times 10^6 B \text{ s}^{-1}$ is the electron gyrofrequency (with B in Gauss). With $n_e \sim 7 \times 10^{13} \text{ m}^{-3}$, $w_{\text{turb}} \sim 0.01$, and $B \sim 1$ G (see Fig. 5), it turns out that $\Omega_{\text{LH}} \sim 7 \times 10^4 \text{ s}^{-1}$ and $\eta_{\text{LH}}^* \approx 3 \times 10^8 \text{ m}^2 \text{ s}^{-1}$,

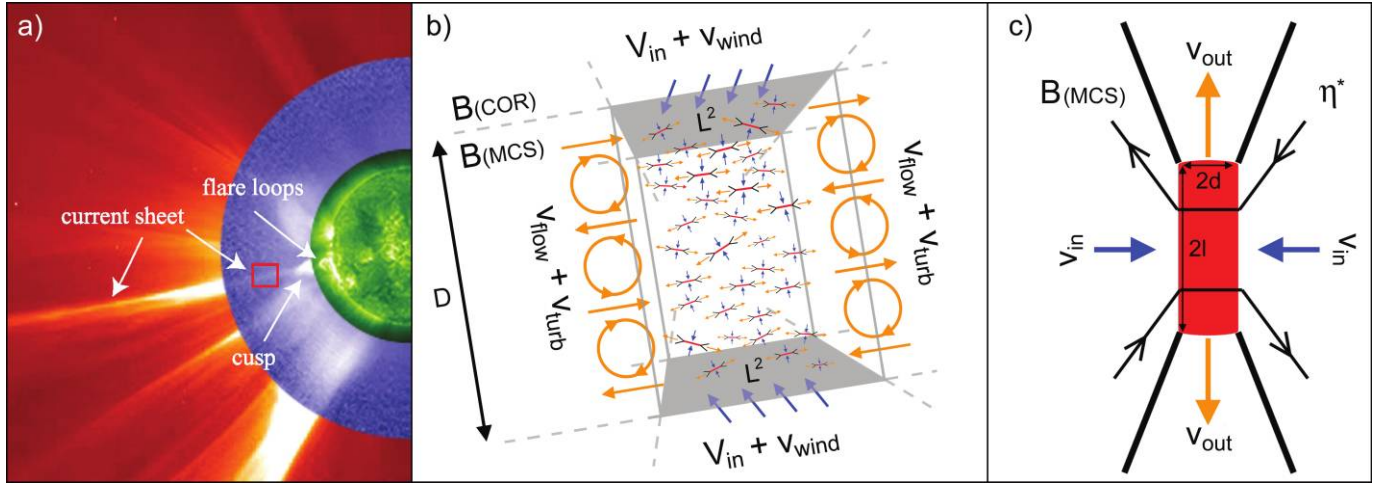


FIG. 7.—Cartoon showing the idea of stochastic reconnection occurring in post-CME CSs. (a) Composite LASCOC/2, Mauna Loa/Mark IV, and EIT/Fe XII image showing the CS related to the CME occurred on 2003 November 18 (adapted from Lin et al. 2005). (b) “Zoom” on the CS part underlined in panel a by a red box, showing the concept of multiple reconnections occurring locally in μCS s located inside the MCS. Inflow toward the MCS occurs with velocity $V_{\text{in}} + v_{\text{wind}}$, while outflow occurs with velocity $v_{\text{flow}} + v_{\text{turb}}$ (see text); the magnetic field changes from the external corona value $B(\text{COR})$ to the MCS value $B(\text{MCS})$. (c) “Zoom” on a single μCS characterized by its inflow v_{in} and outflow v_{out} velocities, its half-length l , and its half-thickness d . Reconnections at local level occur in the ambient plasma characterized by anomalous diffusivity η^* and magnetic field $B(\text{MCS})$; relative sizes are not to scale. Panel a of this figure should be compared with Figs. 1a and 1b.

hence approximately 3 orders of magnitude larger than η_{LH}^* . Values for η_{LH}^* computed at different times are shown in Figure 6 (right panel). Consequences of these value and on the evolution with time of η_{LH}^* will be discussed in § 7.

6. A COMPUTATIONAL TEST: FROM MACRO- TO MICROSCOPIC LEVELS

As mentioned in § 1, a serious problem in the explanation of post-CME CS properties is the huge gap between the expected and the observed values of the CS thickness D . For instance, starting from the average values of $\eta_{\text{IA}}^* \simeq 3 \times 10^5 \text{ m}^2 \text{ s}^{-1}$ and $\eta_{\text{LH}}^* \simeq 3 \times 10^8 \text{ m}^2 \text{ s}^{-1}$ given above and by assuming an inflow speed on the order of $V_{\text{in}} = 10\text{--}100 \text{ km s}^{-1}$, it yields, from the balance between CS diffusion and inflows, an expected CS thickness $D_{\text{IA}} = \eta_{\text{IA}}^*/V_{\text{in}} = 3\text{--}30 \text{ m}$ for the case of IA and $D_{\text{LH}} = \eta_{\text{LH}}^*/V_{\text{in}} = 3\text{--}30 \text{ km}$ for the case of LHD, respectively. These values are some smaller than the observed thickness of white-light post-CME rays ($D \sim 10^4\text{--}10^5 \text{ km}$), usually interpreted as CSs (see, e.g., Webb et al. 2003), and of the spatial extension of the EUV [Fe XVIII] emission ($D \sim 10^4\text{--}10^5 \text{ km}$; see, e.g., Ciaravella et al. 2002; Ko et al. 2003). This gap between macro- and microscopic spatial scales could be filled in the scenario of multiple reconnections occurring in many small-scale regions.

In the following I assume as a computational test that the small-scale reconnection scenario envisaged by some authors for flare-CSs also holds for post-CME CSs, as is shown in Figure 7. However, UVCS observations demonstrated that an important difference with respect to the chromospheric CSs involved in flare reconnection is that plasma flowing along post-CME CSs may undergo a continuous heating even for days after the eruption, while in flare-CSs the energy release occurs on much shorter timescales. Moreover, post-CME CSs extend in the ambient solar corona and hence are immersed in the outflowing solar wind plasma; as a consequence, coronal plasma flowing toward the MCS also transports a momentum parallel to it. LASCOC images revealed that plasma blobs flow along the MCSs with a velocity comparable with that of the solar wind (see Lin et al. 2005), and this could be in agreement with the fact that local reconnections are related to internal forces that preserve the momentum of the inflowing coronal wind plasma. As a consequence local μCS s

(randomly oriented in flare-CSs) will have possibly a preferential orientation parallel to the MCS, as shown in Figure 7, and this implies that the observed [Fe XVIII] line profile broadening will be due mainly to turbulent plasma motions. However, in principle, a contribution due to outflows occurring with a component along the line of sight in the opposite direction of many randomly oriented CSs, as occurs in flare-CSs (see Antonucci et al. 1996), cannot be excluded. In the scenario depicted in Figure 7, magnetic reconnections occur stochastically in many small μCS s spatially uniformly distributed inside the MCS with a preferential orientation parallel to the direction of the coronal magnetic field being dragged in the MCS and locally reconnected and hence parallel to the MCS axis. In the following computation I assume that all the physical parameters (T_e , n_e , B , and η^*) derived in the previous sections are representative of the average ambient plasma inside the MCS where microscopic reconnections occur in μCS s.

If the scenario shown in Figure 7 holds, given the anomalous resistivities η_{IA}^* and η_{LH}^* estimated in the previous sections for IA and LHD instabilities, respectively, it is possible to derive information on the magnetic reconnections occurring in μCS s; to this end, further assumptions are needed. Each μCS will be characterized by its half-length l and half-thickness d , and toward each μCS local inflows and outflows will occur with velocities v_{in} and v_{out} , respectively. The last two quantities are unknown; however, an upper limit to the local inflow speed could be given by the observed v_{turb} and reconnection theory predict that $v_{\text{out}} \simeq v_A$. Hence, in the following the local reconnection rate M_A (i.e., the amount of reconnected magnetic flux per unit time) is computed as $M_A = v_{\text{in}}/v_{\text{out}} \approx v_{\text{turb}}/v_A$ as a fixed quantity, i.e., independent on the above computations of anomalous resistivities. From this assumption it turns out that the M_A upper limit values are on the order of ~ 0.15 (see Fig. 8, top left panel) and increase with time from ~ 0.1 up to ~ 0.2 , because v_A is decreasing faster than v_{turb} (see Fig. 4, bottom right panel; Fig. 5, top left panel). At the local level (see also Fig. 1a) we can write

$$\begin{aligned} v_{\text{in}}l &= v_{\text{out}}d, \\ v_{\text{in}} &= \eta^*/d, \end{aligned} \quad (16)$$

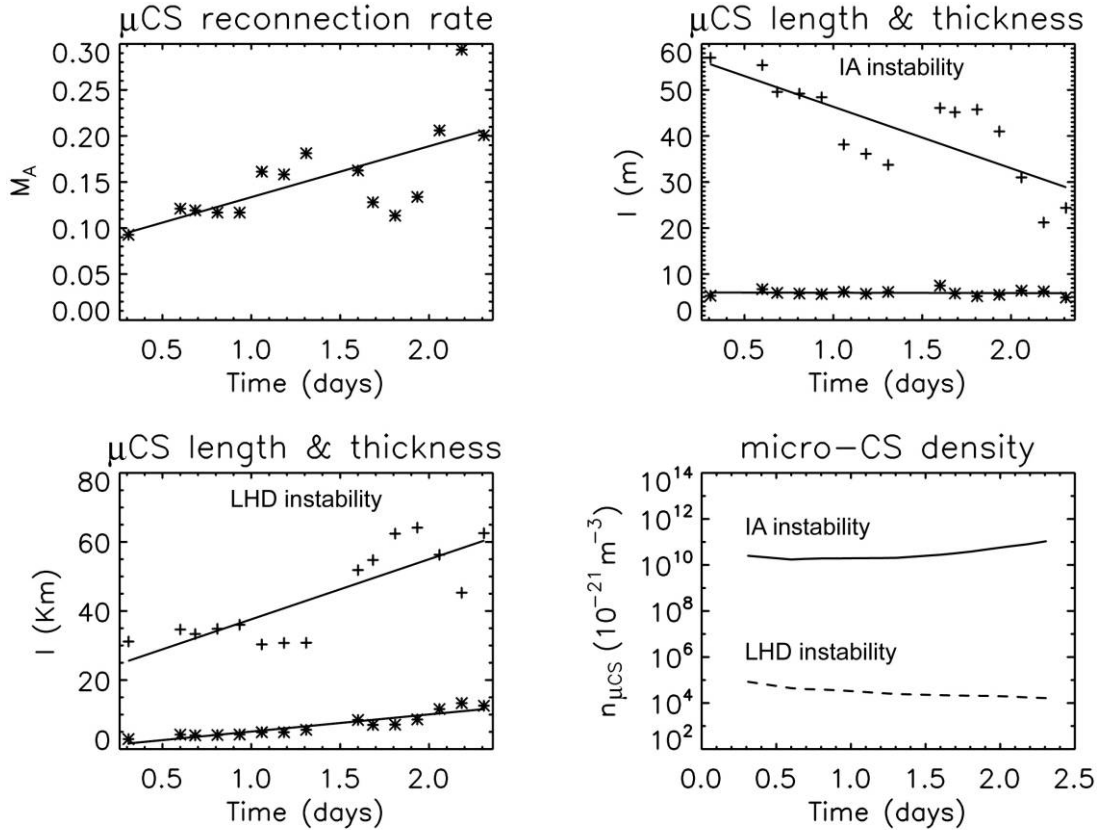


FIG. 8.— *Top left:* Evolution with time of the local reconnection rate $M_A = v_{in}/v_{out}$; values shown in this panel have been computed by assuming $v_{in} \sim v_{turb}$ and hence are an upper limit for real M_A values. Given the local inflow and outflow speeds and the anomalous diffusivity, it is possible to derive the evolution with time of the μ CS half-length l and half-thickness d in the hypothesis of IA (*top right panel*) or LHD instabilities (*bottom left panel*). *Bottom right:* Evolution with time of the μ CS number density $n_{\mu CS}$ (in a volume of 10^{12} km^3) in the hypothesis of IA (*solid line*) and LHD (*dashed line*) instabilities; $n_{\mu CS}$ has been derived by imposing a balance between the energy required to heat the coronal plasma to CS temperatures (adiabatic heating subtracted) and the energy provided by reconnections occurring locally in μ CSs.

where the first equation represents the mass flux conservation and the second equation represents the magnetic energy balance $v_{in}B = \eta^*B/d$. In the first equation the plasma has been assumed to be incompressible; the reason is that in equation (8) the thermal energy increase due to the adiabatic compression along $\Delta\epsilon_\gamma$ has been computed using coronal and MCS densities. This corresponds to the implicit assumption that the coronal plasma flowing toward the MCS region undergoes an adiabatic compression reaching a density $n_e(\text{MCS})$ and a temperature $T_e(\text{COR})[n_e(\text{COR})/n_e(\text{MCS})]^{1-\gamma} \leq T_e(\text{MCS})$. After the adiabatic compression and heating, a further temperature increase up to $T_e(\text{MCS})$ occurs via incompressible magnetic reconnection in the μ CSs. Given v_{in} , v_{out} , and the IA or LHD anomalous resistivity η^* , these equations can be used to estimate the average μ CS half-length l and half-thickness d (i.e., $\lambda_{||}/2$ and $\lambda_{\perp}/2$ in Fig. 1a, respectively).

Results from this computation are shown in Figure 8; the μ CSs have average sizes on the order of $2l_{IA} \sim 80 \text{ m}$ and $2d_{IA} \sim 12 \text{ m}$ for the IA instability, while in the hypothesis of LHD instability μ CSs turn out to be much larger with sizes on the order of $2l_{LH} \sim 90 \text{ km}$ and $2d_{LH} \sim 14 \text{ km}$. This large difference in the μ CS sizes is due in the computation to the ~ 3 orders of magnitude difference between computed values for the IA and LHD anomalous resistivities. Figure 8 also shows a significant difference in the evolution of μ CS sizes depending on the hypothesis of IA or LHD instability; while for IA instability μ CSs have nearly constant thickness and a length decreasing with time, in the hypothesis of LHD instability both μ CS length and thickness increase with time. In the computation this is due to the different

behavior of diffusivities (Fig. 6); η_{IA}^* decreases with time as w_{turb} because $\eta_{IA}^* \propto w_{turb}$ (see eq. [13]), while η_{LH}^* increases with time because $\Omega_{LH} \approx \omega_{pi}(\Omega_e/\omega_{pe})$. Hence, as the magnetic field decreases (Fig. 5, *bottom left panel*), Ω_{LH} decreases faster than w_{turb} , resulting in a η_{LH}^* increase. It is not easy to say, from the theoretical point of view, which one of these two behaviors is more “realistic.” In any case, from the macroscopic point of view all results derived with the above assumptions need to fulfill at least three constraints given by the observations, that is, (1) the observed high MCS temperature evolution, (2) the stationarity of inflows toward the MCS, and (3) the much larger MCS thickness D_{obs} . In the next section it will be discussed how all these conditions can be satisfied in the picture of microscopic reconnections described above.

7. DISCUSSION AND CONCLUSIONS

A first condition that the μ CS scenario described above has to match is the balance between the energy required to heat the coronal plasma up to the MCS temperatures and the energy dissipated by magnetic reconnections occurring in μ CSs. Let us assume that each μ CS occupies a volume $2d \times 2l \times 2l$ (Fig. 7c) that for each μ CS inflow of magnetic energy occurs across a lateral surface $8l^2$. If we consider in the MCS of thickness D a box with volume L^2D (Fig. 7b), then the power $P_{\mu CS}$ dissipated per unit second by μ CSs in this volume is

$$P_{\mu CS} = \frac{B^2(\text{MCS})}{2\mu_0} v_{in} 8l^2 (n_{\mu CS} L^2 D), \quad (17)$$

where $n_{\mu\text{CS}}$ is the unknown μCS number density. This power has to equal the power P_{MCS} required to heat by magnetic reconnections the coronal plasma flowing with velocity V_{in} toward the box L^2D across a surface $2L^2$ (Fig. 7b, shaded area) that is given by

$$P_{\text{MCS}} = \frac{1}{f} (\Delta\epsilon_t - \Delta\epsilon_\gamma) V_{\text{in}} 2L^2, \quad (18)$$

where $\Delta\epsilon_t$ is the total thermal energy increase and $\Delta\epsilon_\gamma$ is the thermal energy increase due to adiabatic compression (see also eq. [8]). By equating $P_{\mu\text{CS}}$ and P_{MCS} , the μCS number density can be estimated as

$$n_{\mu\text{CS}} = \frac{\mu(\Delta\epsilon_t - \Delta\epsilon_\gamma) V_{\text{in}}}{fB^2 2l^2 D} \approx \frac{\mu(\Delta\epsilon_t - \Delta\epsilon_\gamma)}{fB^2 2l^2 D}. \quad (19)$$

By assuming the equality between the global V_{in} and local v_{in} inflow speeds, the above formula gives an order of magnitude estimate of $n_{\mu\text{CS}}$. The resulting values of $n_{\mu\text{CS}}$ are different if we assume that μCS s are produced either by IA or LH instabilities; in particular, equation (19) gives $n_{\mu\text{CS}}(\text{IA}) \sim 4 \times 10^{-11} \mu\text{CS m}^{-3}$ and $n_{\mu\text{CS}}(\text{LH}) \sim 3 \times 10^{-17} \mu\text{CS m}^{-3}$. These densities imply that, for instance, in a volume $(10^4)^3 \text{ km}^3$ inside the MCS a number of μCS s on the order of 4×10^{10} and 3×10^4 for IA and LH instabilities, respectively, is required to provide for the plasma heating that adds to the adiabatic compression heating. The evolution with time of μCS number density is shown in Figure 8 (*bottom right panel*): $n_{\mu\text{CS}}$ is inversely proportional to l^2 ; hence, an increase (decrease) in the length of μCS s (Fig. 8, *top right and bottom left panels*) corresponds to a decrease (increase) in their number density. In this scenario the MCS thermal energy is provided globally by adiabatic compression and locally by incompressible magnetic reconnections; as time goes on, an increase of the local reconnection rate (i.e., the locally reconnected magnetic flux) leads to a faster dissipation of magnetic energy that is “replenished” by coronal inflows at a constant rate. This leads to a decrease in the available magnetic energy density in the MCS, hence in both thermal and turbulent kinetic energies, as observed.

A second condition that has to be matched is the existence of a pressure balance between coronal and MCS plasma able to maintain a stationary inflow of coronal plasma toward the MCS. The MCS thermal pressure is larger than the coronal one; thus, in order to maintain a pressure balance, the unknown coronal magnetic field $B(\text{COR})$ has to be larger than the MCS magnetic field $B(\text{MCS})$ (derived with eq. [8]). Taking also into account the kinetic pressures given by inflow speed V_{in} and wind speed v_{wind} in the corona, and pressures given by turbulent and flow motions v_{turb} and v_{flow} in the MCS, the pressure balance (in MKS units) gives

$$\begin{aligned} 2n_e(\text{COR})k_B T_e(\text{COR}) + \frac{1}{2}\rho(\text{COR})(v_{\text{wind}}^2 + V_{\text{in}}^2) + \frac{B^2(\text{COR})}{2\mu_0} \\ = 2n_e(\text{MCS})k_B T_e(\text{MCS}) + \frac{1}{2}\rho(\text{MCS})(v_{\text{flow}}^2 + v_{\text{turb}}^2) + \frac{B^2(\text{MCS})}{2\mu_0}. \end{aligned} \quad (20)$$

From this equation $B(\text{COR})$ can be estimated; with average values $B(\text{MCS}) = 1.2 \text{ G}$, $n_e(\text{MCS}) = 7 \times 10^{13} \text{ m}^{-3}$, $n_e(\text{COR}) = 1 \times 10^{13} \text{ m}^{-3}$, $T_e(\text{MCS}) = 4 \times 10^6 \text{ K}$, $T_e(\text{COR}) = 1 \times 10^6$, $v_{\text{turb}} = 40 \text{ km s}^{-1}$, $v_{\text{flow}} = 250 \text{ km s}^{-1}$, and by assuming $V_{\text{in}} = 10 \text{ km s}^{-1}$ and $v_{\text{wind}} = 130 \text{ km s}^{-1}$, it turns out on average $B(\text{COR}) \simeq 2.1 \text{ G}$.

The conclusion is that a coronal magnetic field a factor of ≈ 2 larger than the MCS field is sufficient to verify the condition of pressure balance.

The third observational constraint that needs to be reproduced is the much larger thickness of the macroscopic CS (see also the discussion in Ciaravella & Raymond 2008); in the Lazarian & Vishniac (1999) stochastic reconnection model (Fig. 1) only a fraction of the injected magnetic flux is annihilated by ohmic heating within the reconnection zone. In particular, Lazarian & Vishniac (1999) concluded that, if during the process of turbulent reconnection the magnetic energy ϵ_m is injected on some scale l_ϵ with a velocity $v_\epsilon < v_A$, the MCS thickness D_{turb} due to turbulence broadening has to be on the order of

$$D_{\text{turb}} \sim (Hl_\epsilon)^{1/2} \left(\frac{v_\epsilon}{v_A} \right)^2, \quad (21)$$

where $H > l_\epsilon$ is the MCS height (or length) and v_A is the Alfvén speed. Given the μCS sizes $2l$ and $2d$ and number densities $n_{\mu\text{CS}}$ of μCS s for IA and LH instabilities, it is possible to give an order of magnitude estimate for l_ϵ . If we consider a MCS scale length H , in the volume $D_{\text{turb}}H^2$ there are $n_{\mu\text{CS}}D_{\text{turb}}H^2$ μCS s that convert magnetic energy into kinetic and thermal energies. Because each μCS has a lateral surface $S_{\mu\text{CS}}$ on the order of $S_{\mu\text{CS}} = 8l^2$, this means that in the MCS volume $D_{\text{turb}}H^2$ (containing $n_{\mu\text{CS}}D_{\text{turb}}H^2$ μCS s) the magnetic energy is injected through a total surface $S_\epsilon = S_{\mu\text{CS}}n_{\mu\text{CS}}D_{\text{turb}}H^2 = 8l^2n_{\mu\text{CS}}D_{\text{turb}}H^2$ and hence over a scale length $l_\epsilon \approx S_\epsilon^{1/2} = 2Hl(2n_{\mu\text{CS}}D_{\text{turb}})^{1/2}$. Substituting this expression into equation (21) and deriving D_{turb} , it turns out that

$$D_{\text{turb}} \sim 2H^{4/3} (2n_{\mu\text{CS}}l^2)^{1/3} \left(\frac{v_{\text{turb}}}{v_A} \right)^{8/3}, \quad (22)$$

where it has been assumed that $v_\epsilon = v_{\text{turb}}$. Using values $(n_{\mu\text{CS}}l^2)_{\text{IA}} \simeq (n_{\mu\text{CS}}l^2)_{\text{LH}} \simeq 5 \times 10^{-8} \mu\text{CS m}^{-1}$, $v_{\text{turb}} \simeq 40 \text{ km s}^{-1}$, $v_A \simeq 300 \text{ km s}^{-1}$, and assuming $H \sim 0.7 R_\odot$ (i.e., the altitude of the UVCS slit over the solar limb), equation (22) gives $D_{\text{turb}} \sim 1.3 \times 10^4 \text{ km}$ for both IA and LH instabilities. This value is very close to the $D \sim 10^4 \text{ km}$ we assumed in Paper I for the MCS thickness and is in good agreement with other estimates of the MCS thickness.

In conclusion, the main results of this work may be summarized as follows:

1. Previous UVCS studies of post-CME CSs focused mainly on the evolution of UV spectral line intensities, while little information was derived on the line profiles despite their possible relevance in the determination of plasma turbulence. In this work the first comprehensive study on the evolution of the [Fe xviii] profiles observed in post-CME CSs has been conducted.

2. Results show that in all five CSs studied here (at heliocentric distances ranging between 1.5 and 1.7 R_\odot) the [Fe xviii] line is significantly nonthermally broadened. Once the Fe xviii effective kinetic temperatures T_{eff} are plotted as a function of time after the CME occurrence, a general trend appears; T_{eff} is around $\simeq 2 \times 10^7 \text{ K}$ ~ 5 –6 hr after the CME and decreases slowly in the following 2 days down to $\simeq (6$ – $7) \times 10^6 \text{ K}$. At the same time, the electron temperature T_e decreases from $\simeq 8 \times 10^6$ to $\simeq 3 \times 10^6 \text{ K}$.

3. Nonthermal [Fe xviii] line broadening has been ascribed to the turbulence in the CS plasma; it turns out that the T_{eff} decrease corresponds to a turbulence velocity v_{turb} decrease from $\simeq 60 \text{ km s}^{-1}$ (which corresponds to a fraction of turbulent energy density

$w_{\text{turb}} \simeq 1.2\%$) to $\simeq 30 \text{ km s}^{-1}$ ($w_{\text{turb}} \simeq 0.6\%$) in the 2 days after the CME.

4. In the hypothesis that turbulence is due to plasma micro-instabilities, it has been computed that an average fraction of turbulent energy density $w_{\text{turb}} \simeq 0.9\%$ corresponds to an anomalous diffusivity η^* on the order of $\eta_{\text{IA}}^* \simeq 3 \times 10^5 \text{ m}^2 \text{ s}^{-1}$ and $\eta_{\text{LH}}^* \simeq 3 \times 10^8 \text{ m}^2 \text{ s}^{-1}$ for the ion-acoustic (IA) or lower hybrid drift (LHD) instability, respectively.

5. If turbulent reconnection is occurring in many microscopic (thickness of $\sim 10\text{--}10^3 \text{ m}$) current sheets (μCSs) distributed inside the macroscopic (thickness of $\sim 10^4\text{--}10^5 \text{ km}$) structure usually referred as the “current sheet” (MCS), the estimated anomalous diffusivities η^* can be used to infer the size of μCSs . It turns out that average μCS sizes (i.e., length $2l$ and thickness $2d$) are on the order of $2l \sim 80 \text{ m}$, $2d \sim 12 \text{ m}$, and $2l \sim 90 \text{ km}$, $2d \sim 14 \text{ km}$ for IA and LHD instabilities, respectively.

6. With these numbers, the scenario tested here of turbulent reconnection is able to reproduce at macroscopic level at least the following three constraints: (1) the high MCS plasma temperatures (due both to adiabatic compression and reconnections occurring in μCSs), (2) the pressure balance between coronal and MCS plasma (needed to explain the stationarity of MCS), and (3) the much larger observed thickness of MCS (broadened by turbulence).

Note also that the decrease toward 0 of the ambient magnetic field being reconnected (Fig. 5, *bottom left panel*) is in agreement with the result given in Paper I that at the end of observations the plasma heating is provided by adiabatic compression alone (Paper I, Fig. 17).

Hence, the high-temperature emission observed in post-CME CS UVCS spectra even for days after the related eruption is explained here by multiple reconnections occurring continuously at microscopic levels in many small regions in a turbulent ambient plasma. Even if the existence of such μCSs inside the observed macroscopic structures is not demonstrated here, these results suggest that the scenario of turbulent reconnection with anomalous diffusivities is at least able to explain the “scale gap” between the observed and predicted sizes of post-CME CSs in the solar corona.

The author is supported by contract ASI/I/035/05/0. The author thanks ISSI (International Space Science Institute, Bern) for the hospitality provided to the members of the team on *The Role of Current Sheets in Solar Eruptive Events*, where some of the ideas presented in this work have been discussed. In particular, the author thanks Bojan Vršnak for useful discussions. *SOHO* is a mission of international cooperation between ESA and NASA.

REFERENCES

- Amari, T., Luciani, J. F., Aly, J. J., Mikic, Z., & Linker, J. 2003, *ApJ*, 585, 1073
 Antonucci, E., Benna, C., & Somov, B. V. 1996, *ApJ*, 456, 833
 Aschwanden, M. J. 2002, *Space Sci. Rev.*, 101, 1
 Aschwanden, M. J., Kliem, B., Schwartz, U., Kurths, J., Dennis, B. R., & Schwartz, R. A. 1998, *ApJ*, 505, 941
 Bemporad, A., Poletto, G., Suess, S. T., Ko, Y.-K., Schwadron, N. A., Elliott, H. A., & Raymond, J. C. 2006, *ApJ*, 638, 1110
 Birn, J., & Priest, E. R. 2007, *Reconnection of Magnetic Fields* (Cambridge: Cambridge Univ. Press)
 Biskamp, D. 1986, *Phys. Fluids*, 29, 1520
 Brueckner, G. E., et al. 1995, *Sol. Phys.*, 162, 357
 Büchner, J. 2007, *Plasma Phys. Controlled Fusion*, 49, B325
 Büchner, J., & Elkina, N. 2006, *Phys. Plasmas*, 13, 1
 Ciaravella, A., & Raymond, J. C. 2008, *ApJ*, 686, 1372
 Ciaravella, A., Raymond, J. C., & Kahler, S. W. 2006, *ApJ*, 652, 774
 Ciaravella, A., Raymond, J. C., Li, J., Reiser, P., Gardner, L. D., Ko, Y.-K., & Fineschi, S. 2002, *ApJ*, 575, 1116
 Daughton, W. 2003, *Phys. Plasmas*, 10, 3103
 Daughton, W., Lapenta, G., & Ricci, P. 2004, *Phys. Rev. Lett.*, 93, 105004-1
 Davidson, R. C., & Gladd, N. T. 1975, *Phys. Fluids*, 18, 1327
 Hsu, S. C., Fiksel, G., Carter, T. A., Ji, H., Kulsrud, R. M., & Yamada, M. 2000, *Phys. Rev. Lett.*, 84, 3859
 Huang, G., & Lin, J. 2006, *ApJ*, 639, L99
 Huba, J. D., Gladd, N. T., & Papadopoulos, K. 1977, *Geophys. Res. Lett.*, 4, 125
 Ji, H., Terry, S., Yamada, M., Kulsrud, R., Kuritsyn, A., & Ren, Y. 2004, *Phys. Rev. Lett.*, 92, 115001
 Karlický, M., & Bárta, M. 2008, *Sol. Phys.*, 247, 335
 Kim, E.-J., & Diamond, P. H. 2001, *ApJ*, 556, 1052
 Ko, Y.-K., Raymond, J. C., Lin, J., Lawrence, G., Li, J., & Fludra, A. 2003, *ApJ*, 594, 1068
 Kohl, J. L., Noci, G., Cranmer, S. R., & Raymond, J. C. 2006, *A&A Rev.*, 13, 31
 Kohl, J. L., et al. 1995, *Sol. Phys.*, 162, 313
 ———. 1999, *ApJ*, 510, L59
 Kulsrud, R. M. 2001, *Earth, Planets and Space*, 53, 417
 LaRosa, T. N., & Moore, R. L. 1993, *ApJ*, 418, 912
 Lazarian, A., & Vishniac, E. T. 1999, *ApJ*, 517, 700
 Lee, J.-Y., Raymond, J. C., Ko, Y.-K., & Kim, K.-S. 2006, *ApJ*, 651, 566
 Lin, J., & Forbes, T. R. 2000, *J. Geophys. Res.*, 105, 2375
 Lin, J., Ko, Y.-K., Sui, L., Raymond, J. C., Stenborg, G. A., Jiang, Y., Zhao, S., & Mancuso, S. 2005, *ApJ*, 622, 1251
 Lin, J., Li, J., Forbes, T. G., Ko, Y.-K., Raymond, J. C., & Vourlidas, A. 2007, *ApJ*, 658, L123
 Matthaeus, W. H., & Lamkin, S. L. 1985, *Phys. Fluids*, 29(8), 2513
 Norman, C., & Smith, R. 1978, *A&A*, 68, 145
 Parker, E. 1957, *Phys. Rev.*, 107, 830
 Petrosian, V., Donaghy, T. Q., & McTiernan, J. M. 2002, *ApJ*, 569, 459
 Petschek, H. E. 1964, in *Physics of Solar Flares*, ed. W. N. Hess (NASA-SP50), 425
 Priest, E. R. 1982, *Solar Magnetohydrodynamics* (Boston: Reidel)
 Raymond, J. C., Ciaravella, A., Dobrzycka, D., Strachan, L., Ko, Y.-K., Uzzo, M., & Raouafi, N.-E. 2003, *ApJ*, 597, 1106
 Ricci, P., et al. 2005, *Phys. Plasmas*, 12, 055901
 Shibata, K., & Tanuma, S. 2001, *Earth, Planets, and Space*, 53, 473
 Silin, I., & Büchner, J. 2003, *Phys. Plasmas*, 10, 1299
 Smith, D. F., & Priest, E. R. 1972, *ApJ*, 176, 487
 Spitzer, L. 1962, *Physics of Fully Ionized Gases* (London: Interscience)
 Strauss, H. R. 1986, *Phys. Fluids*, 29, 3668
 ———. 1988, *ApJ*, 326, 412
 Sweet, P. A. 1958, in *IAU Symp. 6, Electromagnetic Phenomena in Ionized Gases*, ed. B. Lehnert (Cambridge: Cambridge Univ. Press), 123
 Tajima, T., & Shibata, K. 1997, *Plasma Astrophysics* (Reading: Addison-Wesley)
 Webb, D. F., Burkepile, J., Forbes, T. G., & Riley, P. 2003, *J. Geophys. Res.*, 108, 1440
 Withbroe, G. L., Kohl, J. L., Weiser, H., & Munro, R. H. 1982, *Space Sci. Rev.*, 33, 17
 Wu, G.-P., Huang, G.-L., & Tang, Y.-H. 2005, *Chinese J. Astrophys.*, 5, 99
 Yamada, M. 1999, *J. Geophys. Res.*, 104, 14529